14

Earth Observation for Earthquake Disaster Monitoring and Assessment

Huadong Guo, Liangyun Liu, Xiangtao Fan, Xinwu Li and Lu Zhang
Key Laboratory of Digital Earth Science, Center for Earth Observation and Digital Earth, Chinese Academy of Sciences, Beijing
China

1. Introduction

China is a country where earthquakes and many other disasters happen often. After earthquakes, roads are damaged, traffic is blocked off, secondary disasters occur frequently, weather conditions become adverse, and communications are interrupted, which makes it difficult to gather data from stricken regions. And the big problem for recovery operations is that there is no accurate information about the situation. Earth observation technology, which has many advantages including high-speeds, maneuverability, and macro- to micro-level observation, has shown its importance for gathering information about stricken regions and making reasonable recovery decisions.

Optical Earth observation technology can provide vivid images for target interpretation and disaster information extraction. Maneuverable, flexibile airborne optical observation technology can especially provide real-time surface images, which also obtains information about collapsed houses, broken roads, geological disasters, barrier lakes and so on. It plays an important part in disaster mitigation activities (Guo et al., 2010a). Synthetic aperture radar (SAR) not only has the capability of all-weather monitoring, but also is sensitive to geometric shape and movement, which becomes an efficient tool to analyze and evaluate recent earthquakes (Guo et al., 2000; Guo et al., 2010b). Multi-mode SAR data can provide many kinds of information for disaster research. Wide-mode SAR images and In-SAR images are important methods for detecting terrain deformation. Wide-mode SAR images can analyze the faulted zone and lithologic characteristics in stricken regions from a macro-level, because it acquires large-scale image (Guo et al., 2000). In-SAR images yield information about surface deformation size and spatial distribution acquired from two-scene repeat-pass data (Massonnet & Feigl, 1998). Polarimetric SAR images, due to the sensitivity to target structures, can be used to extract the distribution of collapsed buildings.

After the Wenchuan and Yushu earthquakes, some departments took full advantage of airborne and satellite remote sensing technology, or unmanned aerial vehicles, to obtain images of the disaster area, which played a very important role in disaster emergency monitoring and disaster assessment and reconstruction (Guo et al., 2010ab; Singh et al., 2010; Liou et al., 2010). Besides monitoring targets directly affected by the disaster, such as collapsed buildings (Lei 2009), remote sensing can observe secondary damage such as barrier lakes, collapse, landslide, debris flow et al. (Cui et al, 2008; Wang et al, 2008; Liu et al., 2009; Huang et al., 2009; Ge et al., 2009; Xu et al., 2009; Han et al., 2009; Zhuang et al., 2010; Zhang et al., 2010; Xu et al., 2010).

The Chinese Academy of Sciences (CAS) immediately arranged a cooperative data acquisition program of airborne and satellite remote sensing data after Wenchuan and Yushu earthquakes and obtained 17 categories of more than 500 scenes of satellite images and high-resolution optical and microwave airborne remote sensing data. 8.7 TB of high-resolution data were freely provided initially to 16 ministries and 28 units, and an additional 3.5 TB were later downloaded from the network. At the same time, a study on remote sensing monitoring methods for post-earthquake secondary geological disasters was carried out, which played an important role in the disaster response. This paper focuses on three aspects, including optical Earth observation technology for monitoring secondary geological disasters, multi-mode radar Earth observation for post-earthquake deformation analysis, and an earthquake disaster simulation evaluation system using the results of seismic disaster remote sensing.

2. Detecting geological disasters using optical technology for Earth observation

Optical technology for Earth observation can provide visual images for disaster target interpretation and disaster information extraction. Airborne optical technology is one of the main instruments for Earth observation, with its mobility and flexibility to provide real-time disaster remote sensing and surface images. With disaster mitigation work done to remotely sense secondary disasters after the Wenchuan earthquake, including barrier lake breaches, road damage, and landslides and debris flows, we analyze and discuss technical methods and applications of optical technology for Earth observation in monitoring secondary geological disasters.

2.1 Extracting background information from the disaster area in Wenchuan

The Wenchuan earthquake occurred in the Longmen mountain fault zone. Longmen mountain runs in the general northeast to southeast direction, about 500km from Guangyuan to Ya'an. Longmen mountain is one of China's typical nappe structures, a tectonic rock sheet along a imbricated thrust to the basin mainly formed in the Mesozoic and early Cenozoic (Wang et al, 2001). The Wenchuan earthquake occurred in the crustal brittle-ductile transition zone, and was a shallow earthquake with a focal depth of 10 km to 20 km and longer duration, so its destructiveness was huge (Bi et al, 2008).

After the Wenchuan earthquakes, CAS urgently arranged airborne and satellite data coordinate acquisition plans and obtained 41 scenes of post-disaster, high-resolution satellite data, and 105 scenes of pre-disaster and concurrent high-resolution archive satellite data. An optical remote sensing airplane carrying an advanced ADS40 aviation camera obtained high-resolution (0.5 - 0.8 m) optical pictures of the disaster area totaling 5 TB with a coverage area of 23,000 km^2.

2.2 Remote sensing monitoring and analysis of barrier lakes after the Wenchuan earthquake

High-resolution ADS40 optical images of the disaster area were used to analyze the barrier lake for the first time. In the coverage area, 51 barrier lakes were detected, some with a bead-like distribution. The location, area, water level and height, and area of the dam body were detected according to a monitoring algorithm of barrier lake risk factors and 1:50,000 DEM data. The risk conditions, geology, and distribution of the 51 major barrier lakes were evaluated to support urgent relief work. The research indicated that the distribution of barrier lakes and spatial features of the earthquake fracture zone were identical.

2.2.1 Barrier lake volume detection algorithm

The water level and area of the barrier lakes were first estimated using high-resolution airborne images. The capacity of the barrier lake was then calculated using elevation contours, and the calculation was based on DEM data with a resolution of 25 m, which were interpolated from a 1:50,000-scale topographical map.

The method to calculate the reservoir capacity involves the following steps:

The water surface area was derived from high-resolution airborne images. Then the water surface elevation *(h_s)* was acquired by overlapping the water surface with the DEM data, since the elevation of the water surface is a constant. If there is some small shift between the orthorectified ADS40 image and the DEM data, the interpreted water surface should be adjusted slightly to ensure all interpreted water surfaces' borderline is located at the same altitude. Meanwhile, the elevation of the midline of the river *(h_r)* was directly recorded from the 1:50,000-scale topographic map. Therefore, the elevation difference and the water level could be calculated.

The capacity of the barrier lake was calculated by an integral approach. The capacity V at the water elevation of H is:

$$V(H) = \sum_{i=1}^{n} S_i \times \Delta h \tag{1}$$

where Δh is the integration interval, n is the equally parted cells number of the elevation drop from the water surface elevation *(h_s)* to the elevation of the midline of the river, *(h_r)*, $\Delta h = (h_s - h_r)/n$ is the integration interval of each cell, and S_i is the water surface area at the elevation of $h_r - (i-1)\Delta h$, which can be automatically derived from the DEM data. The capacity and area of all the 51 barrier lakes were calculated by this method. According to their capacities, the barrier lakes were clustered into three types: Type I (large-sized) with a capacity over 3,000,000 m³; Type II (medium-sized) with a capacity between 1,000,000 and 3,000,000 m³; and Type III (small-sized) with a capacity less than 1,000,000 m³

2.2.2 Risk assessment of the barrier lakes

Barrier lakes formed in an earthquake will result in extreme flooding when they burst. Therefore, the risk assessment of barrier lakes becomes very important. The dimensionless blockage index (DBI) was introduced by Casagli and Ermini (Ermini et al, 2003; Liu et al., 2009) to evaluate the stability of a dam:

$$\mathrm{DBI} = log(\frac{A_B \times H_d}{V_d}) \tag{2}$$

where V_d is the volume of the dam, which is the dominant parameter of stability since it determines the gravity of the dam; A_b is the area of the basin, which is the primary parameter of instability since it determines the runoff in the basin; and H_d is the height of the dam, which is an important parameter for evaluating the stability of the barrier lake when confronted with overflow. The smaller the DBI value, the more stable the barrier lake. It is difficult to calculate the dam volume with the remote sensing image without in-situ measurement. An approximate estimation of dam volume is to multiply the dam area with its height, and thus Eq. (2) can be written as:

$$DBI \approx \log\left(\frac{A_b \times H_d}{H_d \times S_d}\right) = \log\left(\frac{A_b}{S_d}\right) \tag{3}$$

where S_d is the dam area.

2.2.3 Detection results of quake lakes in the Wenchuan earthquake

We interpreted the barrier lake surface and the dam area from the high spatial resolution ADS40 airborne images and located the position of the landslide forming the barrier lake. The basin area of the barrier lake was then extracted with the DEM and hydrological data. Therefore, the reservoir capacity and DBI of the barrier lake could be calculated according to Eqs. (1) and (3). The monitoring information of barrier lakes within airborne remote sensing data coverage shows that:

i. Generally, the slope of the landslided are steep, and most of them are over 20 degrees. This condition causes the formation of barrier lakes.
ii. DBI values can reliably reflect the stability of the barrier lakes. A lower DBI value indicates a more stable barrier lake, but the risk of a secondary disaster is higher if breaches and overflows occur. According to the overflow time of the two barrier lakes located at Xiaojia Bridge, Anxian County, and Tangjiashan, Beichuan County, the barrier lakes in the Wenchuan earthquake could survive for more than 30 days if the DBI were smaller than 4.0.
iii. The Wenchuan earthquake generated 10 large-sized and 14 medium-sized barrier lakes. Therefore, immediate attention should be paid to those barrier lakes with serious and continuous breaches.

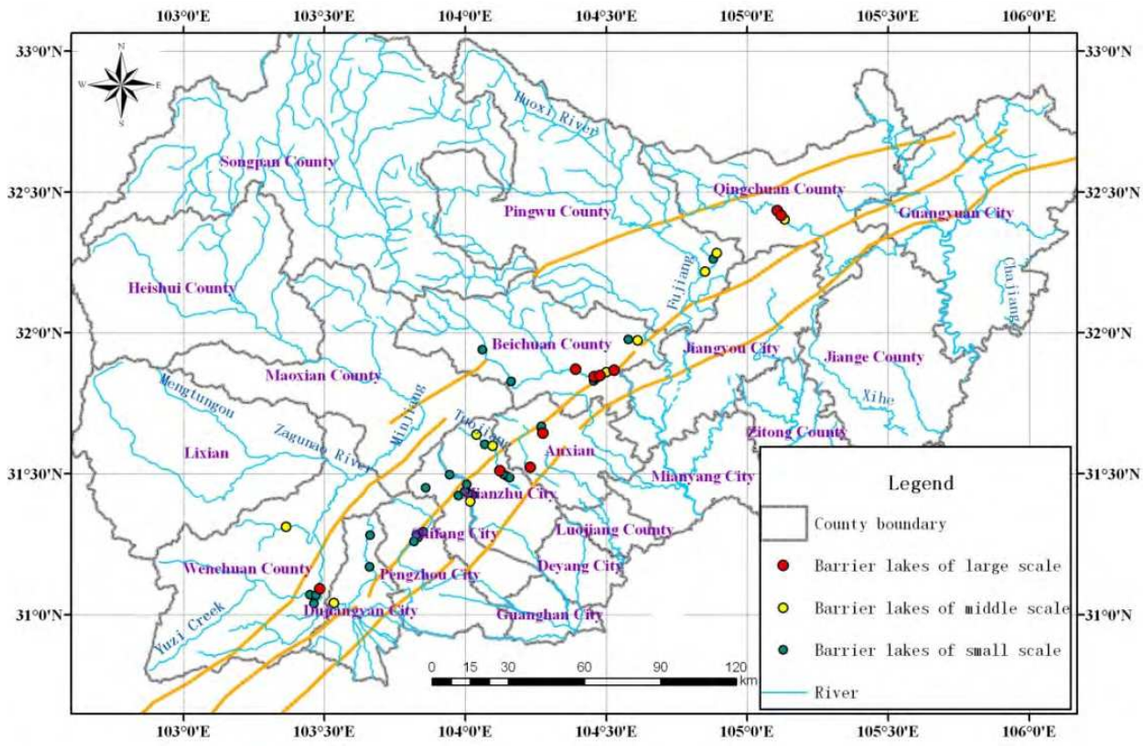

Fig. 1. Distribution map of barrier lakes caused by the Wenchuan earthquake (Liu et al., 2009)

2.2.4 Geological conditions and spatial distribution of the barrier lakes

The Wenchuan earthquake triggered many geological hazards, including collapses and landslides along river valleys. Some of the large masses of land fell into the river valleys and formed a number of barrier lakes. Figure 1 shows the distribution of 51 barrier lakes through the interpretation of remote sensing images. From the distribution map, the barrier lakes were apparently along the Yingxiu-Beichuan fault, and the distribution was consistent with the direction of the fault zone. There were a series of high-risk barrier lakes distributed along the rivers such as the Jianjiang River's upstream in Beichuan County, the Mianyuan River's upstream in Mianzhu City, and the Pingshui River in Shifang City.

2.3 Remote sensing monitoring and analysis of roads damaged by Wenchuan earthquake

High-resolution ADS40 optical airborne remote sensing images and other data were used to analyze and locate some national and provincial highways in seriously damaged areas. The process included analyzing qualitatively, orientatively and quantitatively different factors and classes of blocked and damaged roads from landslip, debris flows, river bank collapse, barrier lakes, earthquake disruption and ground fissuring. These monitoring and analysis results may give transportation department powerful information support.

2.3.1 Road blockage and damage conditions in badly stricken areas

The main remote sensing road blockage and damage condition detection focuses on national and provincial highways. There are 5 national and provincial highways in the badly stricken

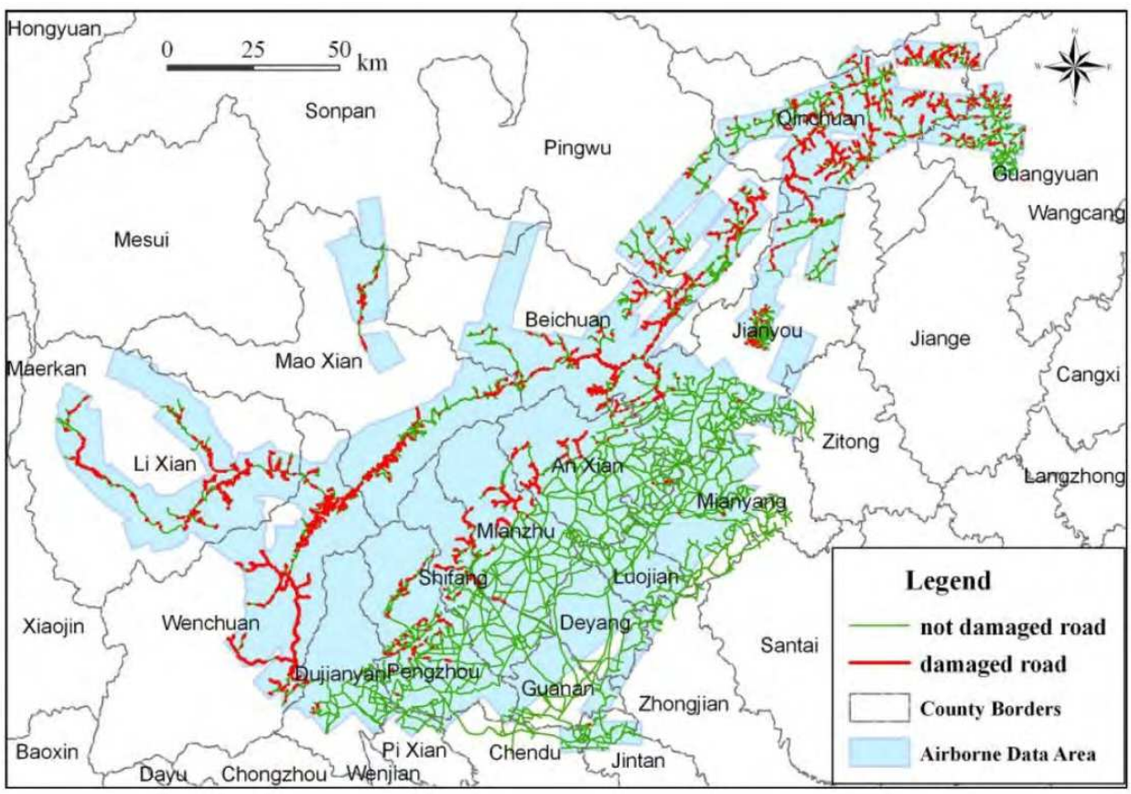

Fig. 2. Map of damaged roads after the Wenchuan earthquake

area, with an overall length of 573.82 km. This includes 3 national roads with a total length of 394.07 km: National Highway 213 (239.563 km) from Xuankou Town, Wenchuan County to Minjiang Village, Mao County, National Highway 212 (31.814 km) from Baolun town, Guangyuan City to Lijia Ping, Qingchuan County, National Highway 317 (122.692 km) from Siboguo Village, Li County to Wenchuan County. It also includes 2 provincial highways with a total length of 179.75 km: Provincial Road 105 (50.85 km) from Anchang Town, An County to Beichuan County and Provincial Road 302 (128.90 km) from Mao County, Jiangyou City.

The Wenchuan earthquake caused more than five national and provincial road blockages and damage, including 808 points in total with a total length of 170.17 km, which accounted for 29.66% of the total length of paths in the badly stricken area, in which, National Road 213 was most seriously damaged, then National Road 317 and Provincial Road 105. Damage to the others was comparatively light. The conditions of damaged roads is described in Figure 2.

2.3.2 Damage level and distribution condition of hard-hit areas

The blocked roads were obviously segmented and the worst parts appeared to have a cluster distribution. Outside of the observed areas, the roads were light damaged and without major disasters such as landslips.

2.3.3 Category, scale and causation of damaged paths

According to remote sensing monitoring and analysis, the blockage paths of the worst-damaged places were caused by geological disasters such as landslips, falling debris, mud-rock flows and ground fissures. The distribution of these disasters was related to the break structure, drape structure, and rock broken under stress.

Fracture tectonic belt was the most important role in road damage. The magnitude-8 earthquake happened on the fault zone of Longmen Mountain, which is composed of many approximately parallel disruptions oriented towards the northeast with a length of more than 500 km and 50 km in width. The Yingxiu-Beichuan fault and Wenchuan-Maoxian fault were the most important parts of the Longmen Mountain fault zone, and the most serious damage to National Road 213 was along these two fault zones.

The background of the badly stricken area's geological structure is very complex with a long evolutionary history. The rocks in hard-hit areas were squeezed extremely because of the long-term activities of well-developed faults and fold faults. These broken rocks provide a large amount of material for potential falling, mud-rock flows (with fragment flows) and landslips. This material slipped rapidly under the force of gravity and piled up on the lower roads and caused blockage in the harder-hit area.

In addition, the earthquake's power is the reason that roads in harder-hit area were blocked and damaged. When the earthquake occurred, there were both southeast-direction thrust extrusion and dextral shear in the Longmen Mountain Fault Zone (Chen Yuntai etc., 2008), which made steep mountains, high-angle clockwise slope and extremely broken rock strata lose their balance and dependence. Then under the action of gravity, broken rock rapidly slid downward, or collapsed and accumulated in low-lying areas on the highway, which damaged and blocked the road.

2.4 Secondary geological disaster analysis of Wenchuan earthquake

Using high-resolution ADS40 optical aviation remote sensing images and comprehensive, conventional data, we evaluated secondary geological disasters, such as collapses,

landslides, and debris flows. Using investigations by remote sensing and field survey results combined with the Ministry of Land and Resources, PRC emergency investigation data, a secondary geological hazards information acquisition model was established. It allowed for the monitoring and rapid extraction of secondary geological disaster data. Researchers studied the characteristics and distribution of secondary geological disasters, completed the interpretation of 11 heavily-damaged area's geologic disasters and their geological background, and analyzed the geological hazards' distribution, intensity, scale and distribution regularity. The study revealed that the development of secondary geological disasters had obvious clustering. In the area, seismic geological hazards were along the Longmen Mountain Fault Zone and mainly caused by the Beichuan-Yingxiuwan fracture control.

2.4.1 Remote sensing information extraction method for secondary geological disasters

The special weather conditions in Wenchuan make the ratio of vegetation coverage higher. The study on vegetation destruction in this area shows the severity of geological disasters and supports the job of disaster evaluation and post-disaster reconstruction.

First, remote sensing data were acquired from before and after the earthquake. Extracting the information map of vegetation was done with standardized resolution and registration. Second, high spatial resolution images were used to check causes of vegetation change including geological disasters, human destruction, agricultural changes and so on. The third step was to remove the vegetation change information caused by non-geological disasters and make a classification according to remote sensing image identification of secondary geological disasters. Last, statistics were calculated and analysis conducted to make a difference map.

i. Standardize resolution and make registration

In order to reduce the extraction difference of vegetation caused by different spatial resolutions, we standardized the spatial resolution of the images by two-dimensional cubic convolution before the vegetation information extraction. Then map-to-map control points were adopted and registered by a polynomial method. Because the registration method uses vegetation information difference extraction before and after the disaster, the registration precision should be controlled within 1 pixel.

ii. extract vegetation information

According to the special vegetation spectrum, we can efficiently extract the vegetation information from pre- and post-disaster images. The formula is as follows:

$$NDVI = \frac{R_{NIR} - R_R}{R_{NIR} + R_R} \tag{4}$$

where NDVI is vegetation index, R_{NIR} is reflectivity of near infrared wave, and R_R is reflectivity of infrared wave. Comparing the results with a real vegetation coverage map to fix the threshold, we can extract the vegetation coverage map and change it into a vector diagram.

iii. extracting the vegetation information difference from geological disasters

Based on the extraction of a vegetation information vector graph, the difference between the two figures can be extracted by doing differential operation. The high spatial resolution data can be used to correct elements caused by the difference and then reject the difference in

vegetation information caused by non-geological factors. Finally, according to remote sensing image identification of secondary geological disasters, they can be classified.

2.4.2 Secondary geological disaster remote sensing monitoring results

The overall results of monitoring secondary geological disaster are shown in Figure 3, where the red stands for landslides, blue for debris flows, and green for collapses. As can be seen from the figure, the landslide occurred mainly in Beichuan, Pingwu and Qingchuan counties; debris flow occurred mainly in Wenchuan, Maoxian and Li counties; and collapse occurred mainly in Wenchuan and Beichuan counties. According to statistics, the total disaster area is about 29,000 square kilometers, and the secondary geological disaster area is 2,250 square kilometers (7.8% of the total).

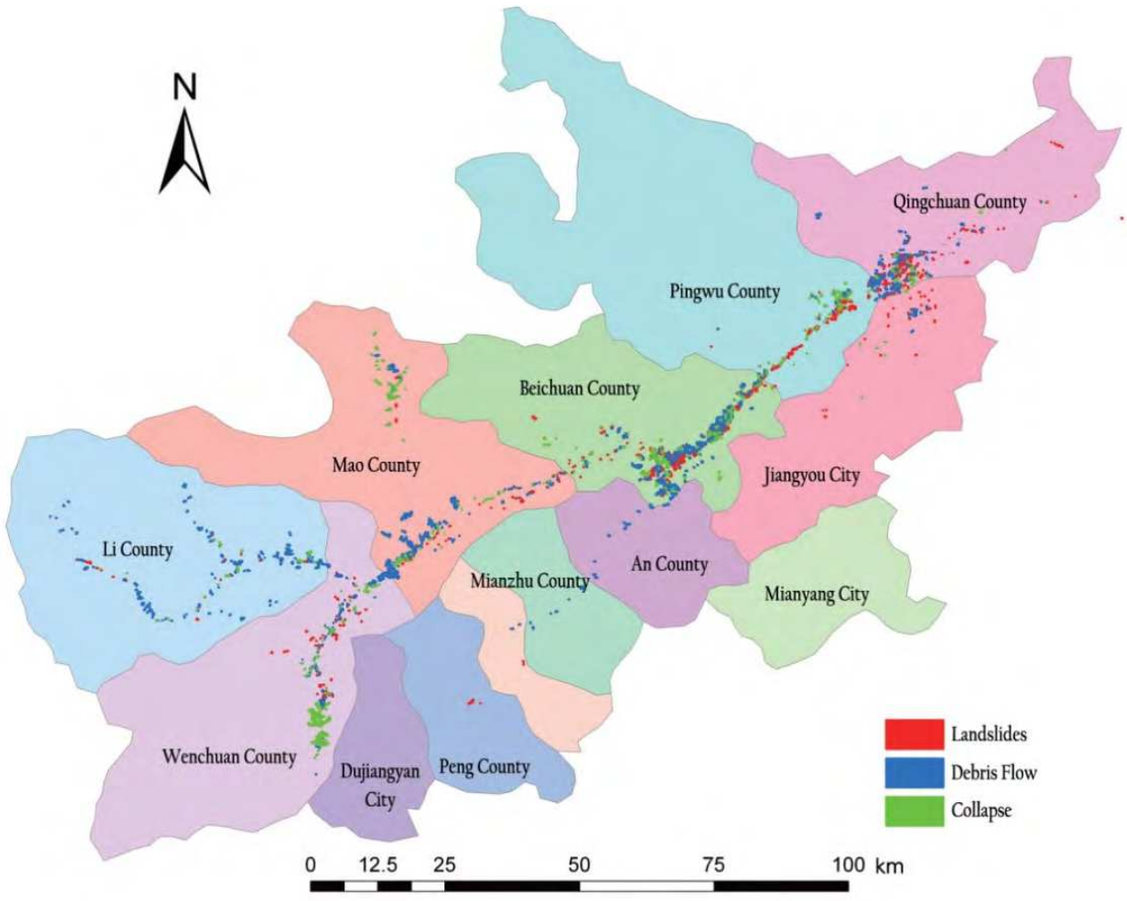

Fig. 3. Map of secondary geological disasters occurring in the heavily-hit areas of the Wenchuan earthquake

3. Multi-mode radar imaging technology for monitoring earthquake deformation

Synthetic aperture radar (SAR) multi-mode data can provide a variety of types of information for earthquake research. We take Yushu earthquake, which occurred in Yushu

County, Qinghai Province, China, on April 14, 2010, as the research object and use RADARSAT-2 and ALOS-PALSAR repeat-pass SAR interferometry data to analyze earthquake deformation characteristics.

3.1 Yushu earthquake area background and data acquisition

The Yushu earthquake occurred in the Garzê-Yushu Fault Zone. The fault strike runs in a northwest direction for a length of nearly 500 km, and has a fracture width from 50 to several hundred meters. From analysis of the plate tectonics, it can be concluded that the source of this earthquake was in the Qinghai-Tibetan Plateau, located in the north of the collision zone in the Himalayas, which was formed by the subduction of the Indian plate toward the Eurasian continent. Because of this plate subduction, lateral sliding of the internal blocks of the Qinghai-Tibetan Plateau occurred, which caused the northward shift of the plateau and its internal blocks and finally, the formation of strike-slip fault systems with different scales at the edge of the blocks. Zhang et al. (2010) inverted the moment tensor solution using wave-form data from global stations. From this solution and the background of the fault tectonics, it can be concluded that the fault with a trend of 119° and a dip of 83° was the earthquake rupture. The breaking process was determined based on teleseismic data from the 35 global stations. Two active regions on the fault surface were identified. One was located near the micro-epicenter, and the other was located to the southeast at a distance of 10 to 30 km. The latter had the greater slip, 2.4 m, and was a near vertical sinistral strike-slip fault.

The study uses SAR data including RADARSAT-2 wide-mode data and ALOS PALSAR repeat-pass data. The RADARSAT-2 wide-mode data was acquired on April 21, 2010, with a spatial resolution of 40 meters and an incident angle of 21 degrees. ALOS PALSAR data, including two pre-earthquake and post-earthquake scenes, were acquired on January 15, 2010, and April 17, 2010, respectively. Table 1 shows the PALSAR data parameters for repeat-pass SAR interferometry.

Sensor	Date	Orbit	Frame	Perpendicular baseline (m)	Temporal baseline (d)
PALSAR	2010-1-15	487	650	700.5	92
PALSAR	2010-4-17	487	650		

Table 1. PALSAR parameters for SAR interferometry

3.2 The method of extracting earthquake geological characteristics and surface deformation information from SAR data

Ground-fissuring phenomena are often a reflection of different lithological characteristics. SAR image brightness and texture structure can reflect the degree of fissuring. In addition, radar waves are sensitive to the linear structure (Guo, 1996, 1997), so using SAR imagery can help interpret tectonic information.

Interferometric SAR is an important means of extracting surface deformation because it can measure it precisely in three-dimensional space, including small deformations of the surface, and can achieve high spatial resolution observation of surface changes in large areas. Interferometric SAR images of the same area at different times by SAR sensor were obtained at different time SAR complex images. Then we process SAR images acquired at different times to obtain an interferogram. SAR interferograms show electromagnetic wave

transmission path length variation from the SAR antenna to the target in two images. Electromagnetic wave transmission path length changes are generally subject to the following three factors: satellite position changes, surface changes, and atmospheric changes. Product by the satellite position changes is terrain interferometry phase, which produced by surface changes is the atmospheric phase. Generally speaking, the SAR interference phase can be expressed as type (5).

$$\Phi_{IFG} = W\left\{\Phi_{topo} + \Phi_{defo} + \Phi_{atm} + \Phi_{noise}\right\} \tag{5}$$

where $W\{\}$ is a phase winding operator, and deformation interference phase in type (5) Φ_{defo} represents monitoring surface deformation ability of SAR interferometry. In order to obtain the deformation interference phase information, the atmosphere in the mathematical model of SAR interference measurement will be classified as noise signal, which directly considers the SAR interferometry phase as the terrain interferometry phase and deformation interference phase (Rosen, 2000), and then the removal of the terrain interferometry phase can obtain surface deformation information.

3.3 Multi-mode SAR data and the Yushu earthquake area evaluation results

3.3.1 Yushu earthquake area lithology and SAR image fraction analysis results

To further analyze the regional earthquake geology, wide-swath RADARSAT-2 SAR data were acquired on April 21, 2010, with HH polarization, a spatial resolution of 40 m, and an incident angle of 21°. Combined with geological data, the study area can be divided into A to E regions (Figure 4).Because radar waves are sensitive to the linear structure (Guo, 1996,

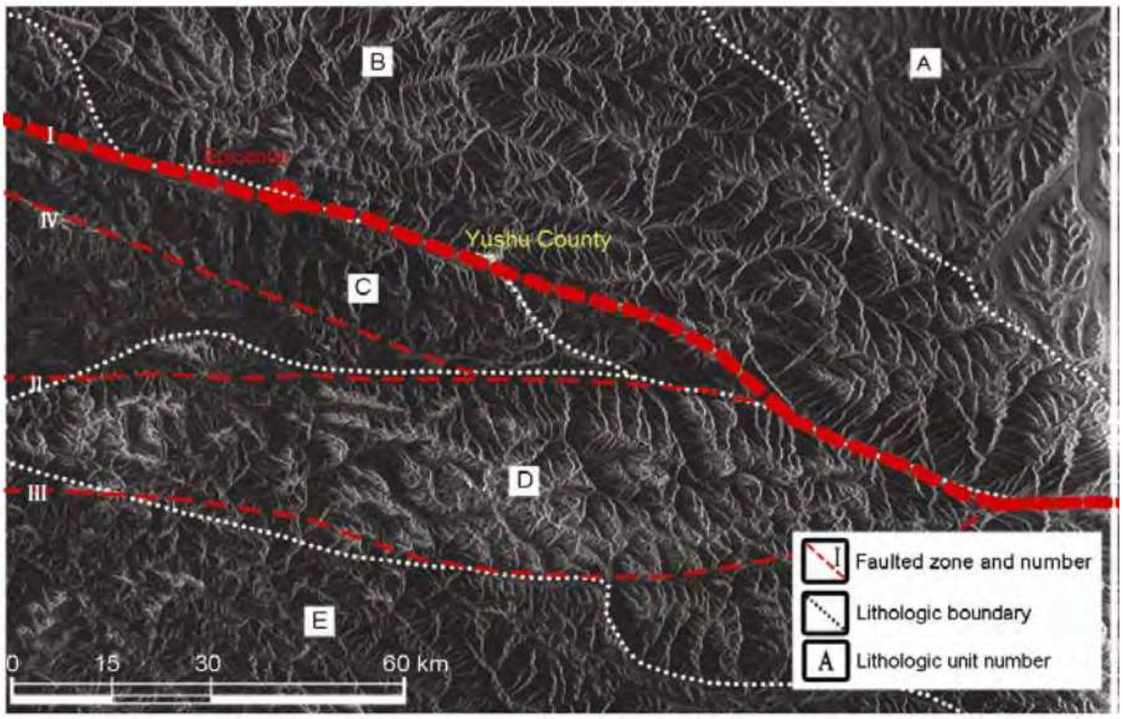

Fig. 4. Geological analysis from RADARSAT-2 HH polarization wide-swath SAR imagery. (from Guo et al., 2010b)

1997), based on the SAR image interpretation and existing research results of active tectonic plates (Deng, 2007), four main faults of this area have been interpreted as follows: the main faults I and IV are oriented in a northwest-southeast direction; fault IV developed in the limestone areas of the map; and faults II and III are distributed in an east-west direction. According to the structural composition of the faults and existing active tectonics results, the main fault I is a strike-slip sinistral fracture.

3.3.2 Yushu earthquake area InSAR deformation extraction analysis result

Using Doris InSAR data processing software and SRTM3 DEM data with 90 m resolution, the two-pass differential interferometry method was used to process the ALOS PALSAR data. We then get the seismic deformation interference phase image shown in Figure 5.

The radar interferogram clearly shows the spatial distribution of the surface deformation field caused by the Yushu earthquake. The coseismic deformation field within the image is about 82 km long and about 40 km wide along the fault. From the distribution of the interferometric fringes caused by the Yushu seismic deformation field, we can see that the distribution of the coseismic deformation is centered on the Garzê-Yushu fault zone, which is the triggered fault (Figure 4, the main fault I), and is parallel to this fault. From the distribution pattern of the interferometric fringes, we can see that the direction and density of the interferometric phase change are different for the two sides of the fault. From the southernmost point A to the fault direction, the interferometric fringe phase indicates an increasing trend from south to north. To the north of the fault, the interferometric fringe phase shows a decreasing trend from north to south. From the whole interferometric phase distribution, the change in the line of sight is left-lateral, revealing significant seismogenic fault sinistral strike-slip properties. It corresponds with the result of wide swath SAR image interpretation.

The seismogenic fault is in a northwest-southeast direction. Along the seismogenic fault zone, there are two major areas with large surface deformation, shown as ① in Figure 5(b) and ② in Figure 5(c). Position ① corresponds with the instrumental epicenter calculated by the National Earthquake Network, and ② corresponds with the macroscopic epicenter. From enlarged views of the interferogram of the instrumental epicenter area in Figure 5(b) and macroscopic epicenter regions in Figure 5(c), we can also see that the radar interferometric fringes change intensely around the instrumental epicenter, while the central region of the macroscopic epicenter has an apparent decorrelation due to the large surface deformation. Both of the two regional seismic fault slip dislocations are relatively large, but that of the latter region, which is close to the city of Yushu, will inevitably lead to stronger tremors for the city of Yushu and the surrounding area, where rupture has been the predominant cause of enormous casualties and economic losses.

PALSAR operates in the L-band, and a color change cycle in the interferogram represents 11.8 cm in the line of sight. According to the interferometric fringes analysis, on the north of the fault, the maximum sinking displacement in the line of sight is 11.8×3=35.4 cm. Since the surface near the epicenter was damaged during the earthquake, the coherence of the corresponding region in the two radar images is very low and cannot form effective interferometric fringes. Therefore, it is reasonable to conclude that one fringe remains on

each side of the fault in the low coherence area, and the cross-fault displacement in the line of sight should not be less than 11.8×8=94.4 cm.

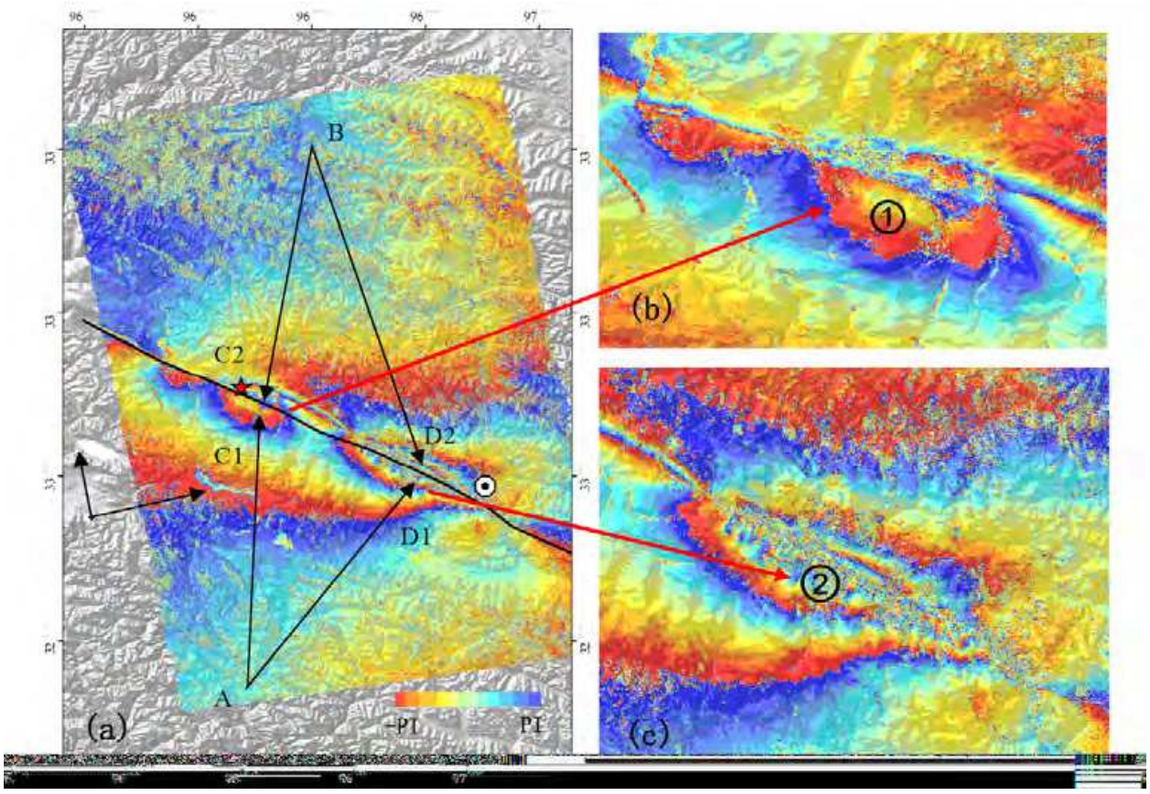

Fig. 5. Coseismic deformation map from ALOS PALSAR data, (a) Differential interferometric phase map; (b) Differential interferometric phase of instrumental epicenter; (c) differential interferometric phase of macro epicenter. A, B, C1, C2, D1 and D2 in (a) represent the different positions and in (b) and in (c) are two large deformation areas (from Guo et al., 2010b).

3.4 Extraction and analysis of collapsed buildings from polarimetric SAR

Large-scale earthquakes severely damage people's lives and property. Fast, accurate, and effective collapsed buildings a monitoring and evaluation after earthquake using remote sensing provides an important scientific basis and decision-making support for government emergency command and post-disaster reconstruction.

RADARSAT-2 polarimetric SAR data (FQ mode, ascending) on April 21, 2010 from Yushu County were used to extract the distribution of collapsed buildings. The resolution of the image is about 8 m and the incidence angle is 21°. From this polarimetric SAR data, the H-α−ρ method (Guo et al., 2010b) was used to extract the spatial distribution of building collapse caused by the earthquake in the Yushu urban area. At the same time, for comparison and analysis, a manual interpretation map obtained from the high-resolution airborne optical image was also collected and shown in Figure 6. From the collapsed buildings extraction result, the reasons for the severe earthquake damage to buildings are also discussed and assessed.

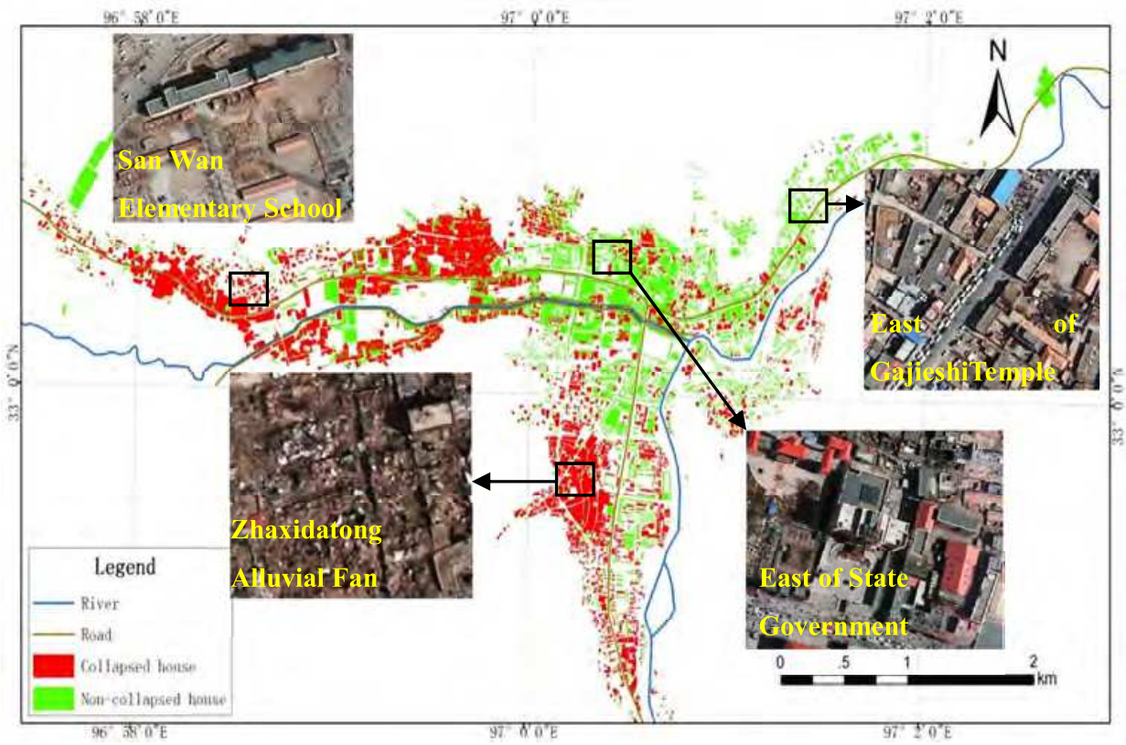

Fig. 6. Spatial distribution of collapsed buildings interpreted from airborne images and sample images for typical regions.

3.4.1 *H–α–ρ* method

From the RADARSAT-2 polarimetric data (FQ mode) and the polarimetric decomposition model, a new *H–α–ρ* method that uses only one post-earthquake SAR image was proposed to identify collapsed buildings. This method mainly utilizes three important polarimetric parameters to extract the collapsed buildings. These parameters are *H*, *α* and *ρ*, Where *H* is entropy, representing the random level of target scattering, *α* is the averaged scattering type and *ρ* is the circle polarization correlation coefficient which is very sensitive to artificial objects. *H* and *α* are obtained by using Cloude's *H–α* decomposition(Cloude, 1996,1997).The *ρ* of uncollapsed buildings is high while that of collapsed buildings is low. However, *ρ* is also related to the surface roughness. For a low roughness surface, the *ρ* is also high. Therefore, it is necessary to remove the disadvantaged influence of the bare soil surface before this parameter can be used for building identification(Ainsworth etc al.,2008). The circular polarization correlation coefficient ρ can be expressed as Eq. 6(F.Mattia, 1997),

$$\rho_{RRLL} = \frac{< S_{RR} S_{LL}^{*} >}{\sqrt{< |S_{RR}|^2 >< |S_{LL}|^2 >}} \tag{6}$$

Where $S_{RR} = iS_{HV} + \frac{1}{2}(S_{HH} - S_{VV})$, $S_{LL} = iS_{HV} - \frac{1}{2}(S_{HH} - S_{VV})$. For the Yushu urban area, three main land cover types were categorized: collapsed buildings, uncollapsed buildings, and bare soil surface. The basic process using *H–α–ρ* method to identify the collapsed buildings is as follows: 1) the extraction of the bare soil surface. *H* and *α* are obtained using

the H–α decomposition theorem, then, the bare soil surface was extracted with H<0.5 and α<42° (Cloude, 1996,1997). 2) Using statistical analysis, the ρ, which can discriminate between uncollapsed and collapsed buildings, is determined. From the high- resolution optical data, typical areas of collapsed and uncollapsed buildings are selected from the radar image to analyze the statistical characteristics of ρ, and the appropriate threshold value of ρ is obtained. 3) From the threshold value of ρ, the separation of collapsed and uncollapsed buildings is conducted, and the distribution map of collapsed buildings is obtained.

3.4.2 Result and analysis of collapsed building extraction

Figure 7 shows the collapsed building distribution of the Yushu urban area extracted by the H–α–ρ method. The rate of building collapse is about 58%. To verify the result, two test sites were selected as follows: (a) a severely damaged area, and (b) an almost undamaged area. Comparing the extraction results with the manual interpretation results from the airborne optical image with a resolution of 0.33 m shown as a' and b' in the lower left corner, we can see that the result of the collapsed buildings' extraction is consistent with the result from the optical manual interpretation. Furthermore, to verify the effectiveness of this method, the recognition rates of collapsed buildings and uncollapsed buildings are analyzed from two sample regions (more than 10000 pixels) from a and b test sites, respectively. From the statistical analysis, the recognition rate for collapsed buildings is 88% and that for uncollapsed buildings is 80%. It should be noted that the polarimetric SAR could play a more important role in the collapsed building extraction if the weather conditions were unsuitable for obtaining optical data.

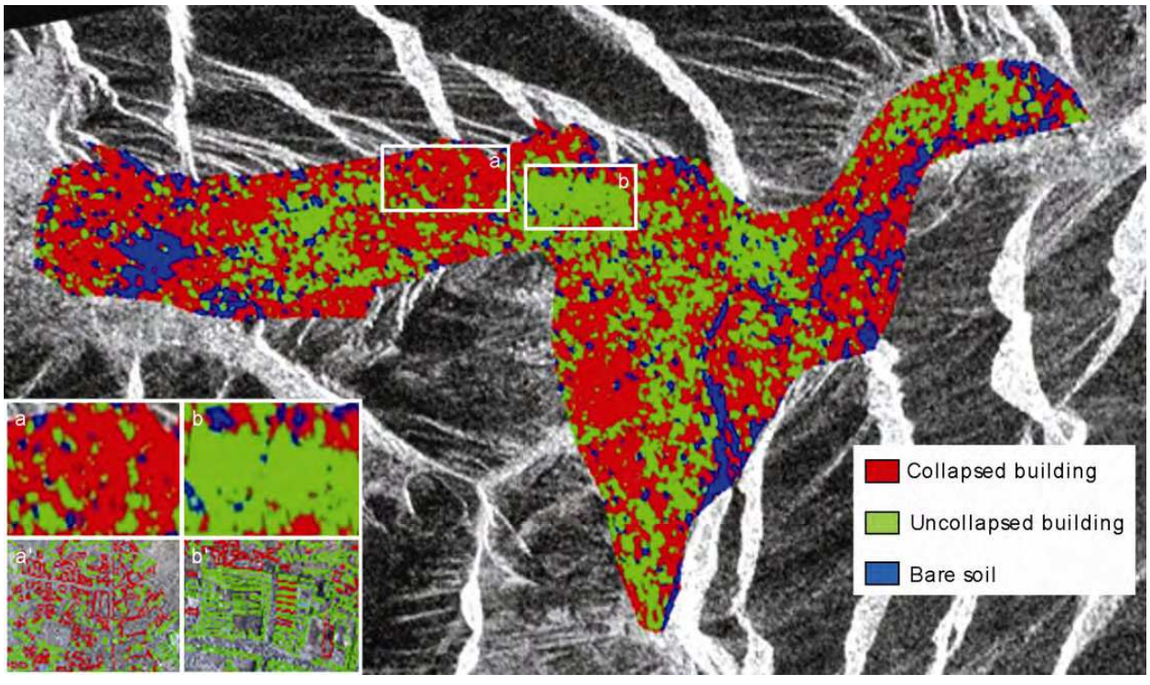

Fig. 7. Collapsed buildings distribution of Yushu County extracted with the H–α–ρ method from polarimetric SAR data, a and b in the lower left corner are the detailed images of the two test sites, a' and b' show the corresponding manual interpretation results from the airborne optical image(from Guo et al., 2010b).

From the collapsed building distribution, it is clear that the degree of collapse is related to the distance from the main fault. The buildings, which were constructed in the alluvial zone, had very poor earthquake resistance because their foundations were weak and most were built of earth and wood.

4. The foundation of an earthquake condition simulation and evaluation system

Based on remote sensing image two-dimensional spatial information systems, interpretation and analysis has been the main means of seismic disaster assessment. Although two-dimensional spatial information systems have the macroscopic and overall characteristics, it also has inevitable defects in the earthquake disaster assessment (Xiao et al, 2001, Li et al, 2007), such as in accurate expression of three-dimensional information, an inability to record non-uniform three-dimensional spatial entities, and a lack of a basis for uneven spatial entity description of lake water, landslides, collapsed buildings and so on. Therefore, it is necessary to establish an evaluation system based on three-dimensional spatial information of earthquake disaster information for analysis.

For the Wenchuan and Yushu earthquakes, using three-dimensional simulation and evaluation with advanced Earth observation technology, we established realistic 3D terrain model using the relatively sophisticated disaster assessment model and successfully created an earthquake disaster simulation and evaluation system. Based on multi-sensor, multi-temporal, and multi-resolution remote sensing images and 1: 50,000 scale DEM data, we produced technology for large 3D terrain modeling and interactive real-time rendering. The 3D simulation system provides a more intuitive disaster analysis method for major collapse, landslide, and debris flow disasters. Using red-blue 3D imaging techniques to get airborne remote sensing stereo images and reconstruct three-dimensional scenes, we can efficiently extract data on damage to housing and improve the disaster analysis accuracy using red and blue stereo glasses. In a 3D environment, not only can the geo-spatial relationship between objects be shown, but also the topological relations between spatial objects. Practice has proven that this kind of three-dimensional assessment is more efficient and reliable.

4.1 Three-dimensional terrain modeling and visualization

We use 1: 50,000 topographic vector data of the disaster area for error analysis and to eliminate gross errors of contour and control point data. We use a difference algorithm for vector contour data to obtain high-resolution DEM raster data. In order to rebuild 3D virtual scenes, we use a merging method of aerial remote sensing images and Landsat TM images to generate the terrain texture. In severe disaster areas, we acquired high-resolution data, TM images. Then combined with DEM data, the aerial remote sensing data can be corrected precisely. Finally, the merging of aviation data and TM data yield the an image of the entire area, which is then mapped to the three-dimensional terrain model to form a virtual 3D environment.

The complicated terrain of earthquake-stricken areas and large data of three-dimension model after overlaying images and DEM have brought challenges for real-time rendering. This paper proposes a multi-resolution triangular grid dynamic geographic model based on computing vision, established a simplified algorithm based on multi-resolution vision. Using a multi-resolution scene model algorithm, this paper resolves the real-time interactive roaming difficulty of large-scale three-dimensional terrain data. First, according to the

amount of data and resolution of images, the magnitude n is established. According to the given format, a model file of different resolutions is generated, and then when modeling real-time rending, a series of irregular grids is used to imitate the terrain. According to their distance from the point of view and complexity of the terrain, we choose the relevant resolution terrain model within sight of the study area that is the closest to the view point. The more complex the terrain is, the higher the terrain series are, the more triangle grids in the drawing area, the more sophisticated the display terrain, and the higher the resolution. Conversely, if the view point is farther away or the terrain is flat, the series of the topography of the area shows will be lower, the number of mesh triangles will be fewer, the terrain rougher, and the resolution lower. Thus, minimizing the number of triangles and reducing memory consumption can make the images and models have identical effects or gaps in a given range, closest to the real terrain.

In this paper we take the improved adaptive quaternary tree to construct layers of details. The quaternary tree index and the grading mode of organization management for large-scale three-dimensional scenes can provide the chance for real-time interactive roaming analysis. In order to ensure the smoothness of scene rendering, we adopt a pre-loaded cache before the scene into the visible range. Then based on real-time rendering of the scene's rectangular range and the quaternary tree index, we can access related scenes' serial numbers quickly, which can be pre-loaded into memory. The scheduling management strategy can improve the rendering efficiency significantly, achieve real time, interactive terrain rendering, and improve the efficiency of disaster evaluation and analysis in the 3D environment.

4.2 Three-dimensional terrain modeling and visualization

Exposed areas along the river valley include a regional north-east-trending thrust fault. The area exhibits many faults and tectonites, which are weak and vulnerable and form the detachment surfaces. Due to the earthquake's physical destruction combined with heavy rain, a large number of landslides, mud-rock flows, and other geological disasters occurred. Our system provides a qualitative and quantitative analysis and monitoring of these secondary disasters. A 3D system for the analysis of secondary disasters has the following advantages:

1. The three-dimensional system can reproduce the true disaster scene, and secondary disasters can be observed directly, including landslides and debris flows and their causes, occurrence and trends (Figure 8a).
2. Using DEM data, the analysis of landslide height and volume can give quantitative estimates of damage due to the scope and extent of landslides.
3. The visual angle can rotate in a 3D system; providing omnidirectional observation of the target, which has obvious advantages in making decisions about rescue routes and strategies.

One example is a statistical analysis of the secondary disaster in Chenjiaba. High-resolution aerial remote sensing images from May 28 were integrated into the system. The system gives information on landslides and mud-rock flows in the area from Beichuan County, Zhixin Village, to Pingwu County Yaogouli. The study identifies the Chenjiaba section landslide debris and other secondary geological disasters as the most serious. The system also marks the distribution of the disaster and builds disaster level categories. There is a total of 135 landslides, covering an area of 508 square kilometers, 38 dilapidations, covering 75.6 square kilometers, and 9 mud-rock flows covering an area of 23.9 square kilometers.

The overlap rate between two adjacent high-resolution images of the disaster area from airborne remote sensing is high. Using this characteristic and remote sensing image processing, the images can generate red and blue stereopairs. Through red and blue stereo glasses, they can show the 3D Spatial Information of buildings in the disaster area intuitively and greatly improve the identification and extraction efficiency of housing damage information. The identification accuracy of semi-damaged buildings increases to more than 10%.

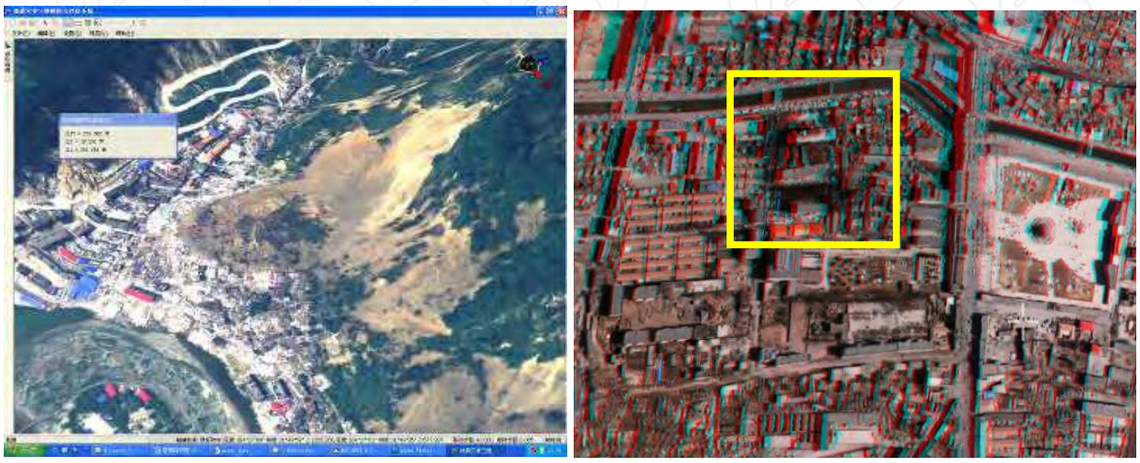

(a) (b)

Fig. 8. (a) 3D analysis of secondary geological disasters in the Wenchuan earthquake, (b) 3D view in red-blue mode for damaged building extraction.

5. Conclusion

Remote sensing monitoring of the Wenchuan and Yushu earthquakes' secondary geological disaster shows that high-resolution optical remote sensing, which can extract the seismic secondary disaster remote sensing characteristics accurately and monitor and evaluate the information of spatial distribution, damage degree and so on of earthquake secondary geological disasters has some advantages, such as intuition, large information and quantification. SAR has the advantages of all-weather data acquisition. The Yushu earthquake multi-mode SAR remote sensing monitoring study has proven that multi-mode SAR is effect and has important potential in earthquake disaster analysis and evaluation. Three-dimensional computing technology for measuring secondary geological disasters is an important technology, which not only improves the calculation and simulation accuracy of secondary geological disasters, but also can promote collaboration on three-dimensional simulation technology and auxiliary mitigation and provide analysis platforms for interactive operation in secondary geological disasters.

In addition, quantitative and reliable evaluation of secondary earthquake disaster depends on high-resolution Earth observation technology. But at present the automatic disaster monitoring algorithms and software for high-resolution Earth observation images still cannot meet actual needs, and 3D interactive analysis platform technology is still not mature. Meanwhile, secondary geological disaster monitoring relies heavily on traditional man-machine interactive visual interpretation technology.

6. Acknowledgement

The authors would like to thank all of the team members who participated in the Wenchuan Earthquake Disaster Reconstruction, Monitoring and Assessment Using Remote Sensing Technology.

This work was supported by the National Basic Research Program of China (2009CB723906, 2009CB723902) and National Natural Science Foundation of China (60972141).

7. References

Ainsworth T L, Schuler D L, Lee J S. Polarimetric SAR characterization of man-made structures in urban areas using normalized circular-pol correlation coefficients. Rem Sens Environ, 2008, 112: 2876–2885

Chen Yuntai, Xu Lisheng, Zhang Yong et al., Report on the Wenchuan large earthquake source of May 12, 208, http://www.csi.ac.cn/Sichuan

Cloude S R, Pottier E. A review of target decomposition theorems in radar polarimetry. IEEE Trans Geosci Rem Sens, 1996, 34: 498–518

Cloude S R, Pottier E. An entropy based classification scheme for land applications of polarimetric SAR. IEEE Trans Geosci Rem Sens, 1997, 35: 68–78

Cui Peng, Wei Fangqiang, He Siming et al. 2008. Mountain disasters induced by the earthquake of May 12 in Wenchuan and the disasters mitigation. JOURNAL OF MOUNTAIN SCIENCE, 26(3):.280-282(In Chinese)

Deng Qidong, Ran Yongkang, Yang Xiaoping. 2007. Active tectonic map of China. Beijing: Earthquake Press (In Chinese)

Ermini L. and Casagli N. 2003. Prediction of the behavior of landslide dams using a geomorphological dimensionless index. Earth Surface Processes and Landforms, 28(1): 31-47.

F.Mattia, T.Le Toan, J. C.Souyris, G.D.Carolis, N.Floury,and F.Posa, The effect of surface roughness on multifrequency polarimetric SAR data . *IEEE Trans Geosci Rem. Sens.*, vol. 35, no. 4, pp. 954−966, July 1997

Fu Bihong, Shi Pilong, Zhang Zhilong. 2008. Spatial characteristics of the surface rupture rroduced by the MS 8.0 Wenchuan earthquake using high-resolution remote sensing imagery. ACTA GEOLOGICA SINICA, 82(12): 1679-1687(In Chinese)

Ge Yong, Xu Jun, Liu Qingsheng, et al. 2009. Image interpretation and statistical analysis of vegetation damage caused by the Wenchuan earthquake and related secondary disasters. Journal of Applied Remote Sensing, 3, 031660.

Guo H D, Liao J J,Wang C L et al. 1997. Use of multifrequency,multipolarization shuttle imaging radar for volcano mapping in the kunlun mountains of western China. Remote Sensing of Environment, 59:364-374.

Guo H D, Zhu L P,Shao Y et al. 1996. Detection of structural and lithological features underneath a vegetation canopy using SIR-C/X-SAR data in Zhao Qing test site of southern China. Journal of Geophysical Research, 101(E10): 23101-23108.

Guo Huadong, Liu Hao, Wang Xinyuan, et al. 2000. Subsurface old drainage detection and paleoenvironment analysis using spaceborne radar images in Alxa Plateau, Science in China Series D: Earth Sciences, 43(4): 439-448.

Guo Huadong, Liu Liangyun, Lei Liping, et al. 2010a. Dynamic analysis of the Wenchuan Earthquake disaster and reconstruction with 3-year remote sensing data, International Journal of Digital Earth, 3(4):355–364.

Guo Huadong, Wang Xinyuan, Li Xinwu, et al.. 2010b. Yushu earthquake synergic analysis using multimodal SAR datasets. Chinese Science Bullet, 55(31): 3499-3503.

Guo Huadong. 2000. Radar for Earth observation: Theory and Applications, Beijing: Science Press(In Chinese)

Han Yongshun, Liu Hongjiang, Cui Peng, et al. 2009, Hazard assessment on secondary mountain-hazards triggered by the Wenchuan earthquake. Journal of Applied Remote Sensing, 3, 031645.

Huang Xiaoxia, Wei Chenjie, and Li Hongga. 2009. Remote sensing analysis of the distribution and genetic mechanisms of transportation network damage caused by the Wenchuan earthquake. Journal of Applied Remote Sensing, 3, 031650.

Jin Feng, Shen Xuhui, Hong Shunying, Ouyang Xinyan. 2008. The application of remote sensing in the earthquake science research. Remote Sensing for Land&Resources, (2): 5—8(In Chinese)

Lei Liping, Liu Liangyun, Zhang Li, et al. 2009. Assessment of spatial variation of the collapsed houses in Wenchuan earthquake with aerial images. Journal of Applied Remote Sensing, 3, 031670.

Li ping, Tao xiaxin, Yan shiju. 2007. 3S-based quick evaluation of earthquake damage, Journal of natural Disasters, 16(3):110-113 (In Chinese)

Liou Yuei-An, Kar Sanjib K.; Chang Liyu. 2010. Use of high-resolution FORMOSAT-2 satellite images for post-earthquake disaster assessment: a study following the 12 May 2008 Wenchuan Earthquake. International Journal of Remote Sensing, 31(13):3355 – 3368.

Liu Liangyun, Wu Yanhong, Zuo Zhengli, et al.. 2009. Monitoring and assessment of barrier lakes formed after the Wenchuan earthquake based on multitemporal remote sensing data. Journal of Applied Remote Sensing. 3, 031665.

Massonnet D., Feigl K. 1998. Radar interferometry and its application to changes in the Earth's surface. Reviews of Geophysics, 36(4):441-500.

Paul Rosen, Scott Hensley, Ian R. Joughin, et al. 2000. Synthetic aperture radar interferometry. Proceedings of the IEEE, 88(3):333–382

Ramesh P. Singh. 2010. Satellite observations of the Wenchuan Earthquake, 12 May 2008. International Journal of Remote Sensing, 31(13):3335 – 3339.

Wang Erqi, Zhou Yong, et al. 2001. Geologic and geomorphic origins of the east Himalayan gap. Chinese Journal of Geology (SCIENTIA GEOLOGICA SINICA), 36(1):122-128(In Chinese)

Wang Shixin, Zhou Yi, Wei Chengjie, ShaoYun, Yan Fuli. 2008. Risk Evaluation on the secondary disasters of dammed lakes using remote sensing datasets，in the‘Wenchuan Earthquake. Journal of Remote Sensing, 12(6):900-907(In Chinese)

Xiao lebin, Zhong ershun, Liu jiyuan, Song guanfu, 2001, A Disussion on Basic Problems of 3D GIS, Journal of Image and Graphics, 6(9): 842-848. (In Chinese)

Xu Min, Cao Chunxiang, Zhang Hao, et al. 2010. Change detection of an earthquake-induced barrier lake based on remote sensing image classification. International Journal of Remote Sensing, 31(13): 3521 – 3534.

Xu Weihua, Dong Rencai, Wang Xuezhi, et al. 2009. Impact of China's May 12 earthquake on Giant Panda habiat in Wenchuan County. Journal of Applied Remote Sensing, 3, 031655.

Zhang Wenjiang, Lin Jiayuan, PengJian, et al. 2010. Estimating Wenchuan Earthquake induced landslides based on remote sensing. International Journal of Remote Sensing, 31(13): 3495 – 3508.

Zhang Yong, Xu Lisheng, Chen Yuntai, et al. 2010. Fast inversion of rupture process for 14 April 2010 Yushu, Qinghai, earthquake. Acta Seismologica Sinica, 32(3): 361-365(In Chinese)

Zhuang JianQi, Cui Peng, Ge YongGang, et al. 2010. Probability assessment of river blocking by debris flow associated with the Wenchuan Earthquake. International Journal of Remote Sensing, 31(13):3465 – 3478.

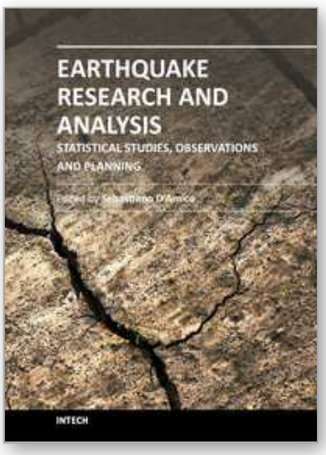

Earthquake Research and Analysis - Statistical Studies, Observations and Planning

Edited by Dr Sebastiano D'Amico

ISBN 978-953-51-0134-5
Hard cover, 460 pages
Publisher InTech
Published online 02, March, 2012
Published in print edition March, 2012

The study of earthquakes plays a key role in order to minimize human and material losses when they inevitably occur. Chapters in this book will be devoted to various aspects of earthquake research and analysis. The different sections present in the book span from statistical seismology studies, the latest techniques and advances on earthquake precursors and forecasting, as well as, new methods for early detection, data acquisition and interpretation. The topics are tackled from theoretical advances to practical applications.

How to reference

In order to correctly reference this scholarly work, feel free to copy and paste the following:

Huadong Guo, Liangyun Liu, Xiangtao Fan, Xinwu Li and Lu Zhang (2012). Earth Observation for Earthquake Disaster Monitoring and Assessment, Earthquake Research and Analysis - Statistical Studies, Observations and Planning, Dr Sebastiano D'Amico (Ed.), ISBN: 978-953-51-0134-5, InTech, Available from: http://www.intechopen.com/books/earthquake-research-and-analysis-statistical-studies-observations-and-planning/earth-observation-for-earthquake-disaster-monitoring-and-assessment

INTECH
open science | open minds

InTech Europe
University Campus STeP Ri
Slavka Krautzeka 83/A
51000 Rijeka, Croatia
Phone: +385 (51) 770 447
Fax: +385 (51) 686 166
www.intechopen.com

InTech China
Unit 405, Office Block, Hotel Equatorial Shanghai
No.65, Yan An Road (West), Shanghai, 200040, China
中国上海市延安西路65号上海国际贵都大饭店办公楼405单元
Phone: +86-21-62489820
Fax: +86-21-62489821

IntechOpen